Neelmeijer, J., Motagh, M., Bookhagen, B. (2017): High-resolution digital elevation models from single-pass TanDEM-X interferometry over mountainous regions: A case study of Inylchek Glacier, Central Asia. - *ISPRS Journal of Photogrammetry and Remote Sensing*, *130*, pp. 108—121.

DOI: http://doi.org/10.1016/j.isprsjprs.2017.05.011

High-resolution digital elevation models from single-pass TanDEM–X interferometry over mountainous regions: A case study of Inylchek Glacier, Central Asia

Julia Neelmeijer[a,b,*], Mahdi Motagh[a,c], Bodo Bookhagen[b]

[a] *GFZ German Research Centre for Geosciences, Section 1.4 Remote Sensing, Telegrafenberg, 14473 Potsdam, Germany*
[b] *Institute of Earth and Environmental Science, University of Potsdam, 14476 Potsdam, Germany*
[c] *Institute of Photogrammetry and GeoInformation, Leibniz University Hannover, 30167 Hannover, Germany*

Abstract

This study demonstrates the potential of using single-pass TanDEM–X (TDX) radar imagery to analyse inter- and intra-annual glacier changes in mountainous terrain. Based on SAR images acquired in February 2012, March 2013 and November 2013 over the Inylchek Glacier, Kyrgyzstan, we discuss in detail the processing steps required to generate three reliable digital elevation models (DEMs) with a spatial resolution of 10 m that can be used for glacial mass balance studies. We describe the interferometric processing steps and the influence of a priori elevation information that is required to model long-wavelength topographic effects. We also focus on DEM alignment to allow optimal DEM comparisons and on the effects of radar signal penetration on ice and snow surface elevations. We finally compare glacier elevation changes between the three TDX DEMs and the C–band shuttle radar topography mission (SRTM) DEM from February 2000. We introduce a new approach for glacier elevation change calculations that depends on the elevation and slope of the terrain. We highlight the superior quality of the TDX DEMs compared to the SRTM DEM, describe remaining DEM uncertainties and discuss the limitations that arise due to the side-looking nature of the radar sensor.

*Corresponding author, E-mail: neelmeijer@gfz-potsdam.de

Keywords: TanDEM–X, InSAR, DEM generation, inter-annual glacier elevation change, Inylchek Glacier

1. Introduction

Glacial and geodetic mass balance measurements are important for quantifying glacial processes and their relationships to climate change, water availability, and sea level rise (Hagg et al., 2004; Fischer, 2011; Zemp et al., 2013). However, collecting in situ data at remote glaciers is time-consuming, expensive and often associated with logistical difficulties (Bhambri et al., 2011; Yan et al., 2013). Digital elevation models (DEMs) that are generated from satellite remote sensing data are a powerful tool to infer glacier elevation changes in mountainous areas (Racoviteanu et al., 2007; Paul and Haeberli, 2008; Friedt et al., 2012).

In June 2010, the TanDEM–X (TDX) satellite was launched to enable, along with its twin TerraSAR–X, the generation of a new global DEM with an unprecedented spatial resolution of 12 m in the horizontal direction and a relative height accuracy of 2 m (Krieger et al., 2013). To date, the promising potential of TDX DEMs for investigations of glacier elevation changes in comparison to other remote sensing-based elevation data has been shown mainly in regions of large ice-sheets, e.g. in Antarctica (Groh et al., 2014; Rott et al., 2014; Seehaus et al., 2015; Wuite et al., 2015) and in Greenland (Bevan et al., 2015). In contrast to low-relief areas, DEM generation from interferometry is difficult in high mountainous terrain, which is one reason that few assessments based on TDX imagery are available. Example studies are from the Himalaya (Pandey and Venkataraman, 2013; Vijay and Braun, 2016), the Purogangri Ice Cap on the Tibetan Plateau (Neckel et al., 2013), the Karakoram (Rankl and Braun, 2016) and the Southern Patagonia Icefield (Jaber et al., 2013).

Most of these studies measure glacier elevation changes on the decadal timescale by subtracting a TDX DEM and a second DEM from a different data source. The C–band Shuttle Radar Topography Mission (SRTM) DEM from February 2000 is usually used as a reference DEM, but this timescale does

not allow the identification of elevation changes on shorter time intervals. We aim to extend the approach by comparing multiple high-resolution (10 m) TDX DEMs to assess annual elevation changes in a high-mountain region. We focus our efforts on detailed descriptions of the processing steps, accuracy assessment, and limitations that arise from the side-looking nature of the radar acquisitions.

The TDX DEM generation process is illustrated using the example of the Inylchek Glacier, which is a valley glacier located in the Pobeda–Khan Tengri massif in the Central Tien Shan mountain range (Fig. 1). It consists of two heavily debris-covered branches, the Northern and Southern Inylchek, which are separated by the Khan Tengri mountain range (6995 m a.s.l.; Glazirin (2010)) and the subglacial Lake Merzbacher. According to the glacier outline from 2000, Southern Inylchek is approximately 60 km long and covers an area of 508 km^2 with elevations ranging between 2860 and 7080 m a.s.l., and Northern Inylchek is approximately 33 km long and covers an area of 159 km^2 between elevations of 3300 and 6600 m a.s.l. Most of the accumulation on the glacier occurs during the summer months (Aizen et al., 1997, 2006). Its equilibrium line (ELA) is located at approximately 4500 m a.s.l. (Aizen et al., 2007). Thick debris covers the lower ablation areas and shields the ice from the sun's radiation, which led to only a minor loss of area of 1.4% between 1990 and 2010 (Osmonov et al., 2013). Both branches of the glacier flow in an east-west direction, which is fortunate for radar sensors that follow a polar orbit. However, the main tributaries of Southern Inylchek are oriented north-south, and thus are heavily affected by layover and shadowing effects.

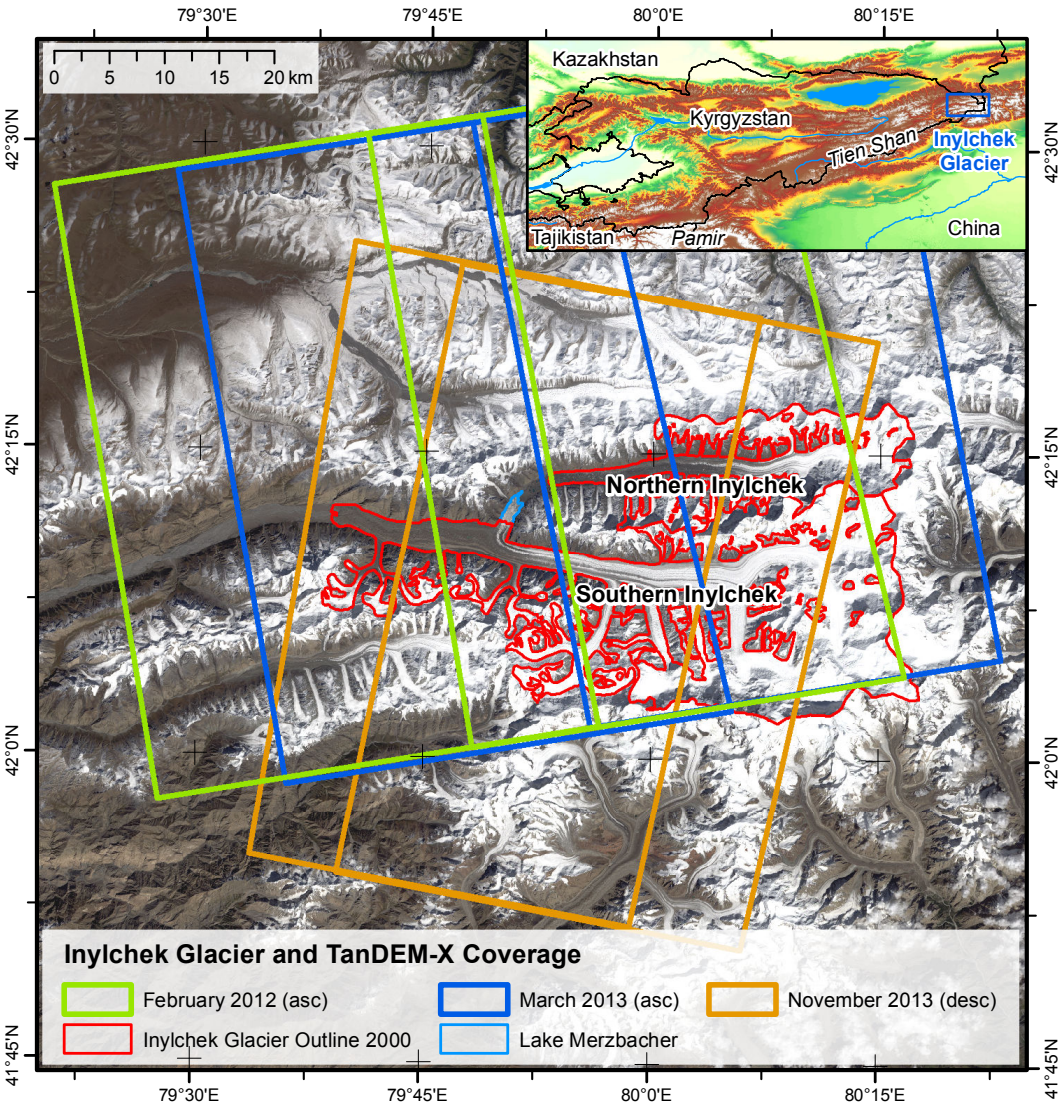

Figure 1: Geographic setting of the Inylchek Glacier showing the Northern and Southern Inylchek branches and Lake Merzbacher on a Landsat 8 imagery from 12 September 2014 (RGB channels: 4-3-2). The coverage and timing of the TanDEM–X radar acquisitions are highlighted with different colours (asc and desc refer to ascending and descending, respectively). Adjacent pairs are illustrated by the same colour. The small inset shows the location of Inylchek on the border between Kyrgyzstan and China.

The Inylchek Glacier has been the subject of numerous studies. Erten et al. (2009); Li et al. (2013, 2014) and Nobakht et al. (2014) focused on the general flow dynamics, whereas Mayer et al. (2008); Neelmeijer et al. (2014) and Zech et al. (2015, 2016) investigated the glacier's flow regime but specifically addressed the relationship to the regularly occurring glacial lake outburst floods from Lake Merzbacher. The unique setting of Lake Merzbacher has been analysed using several modelling approaches (Konovalov, 1990; Ng et al., 2007; Ng and Liu, 2009; Kingslake and Ng, 2013; Mayr et al., 2014). The glacier has also been included in regional mass balance studies (Farinotti et al., 2015; Pieczonka and Bolch, 2015; Shangguan et al., 2015).

2. Data

In this section, we provide an overview of the TanDEM–X Coregistered Single look Slant range Complex (CoSSC), external DEM and glacier boundary data sets that were used in this study. The abbreviations of the DEM data are listed in Table 1.

Table 1: Naming conventions, origins and default resolutions of the DEMs used in this study. The SRTM DEM data were acquired between 11. and 22. February 2000. The exact acquisition dates for the mosaicked TDX DEMs are given in Table 2.

Abbreviation	DEM	Origin	resolution
SDX	X–band SRTM DEM from DLR	©DLR/ASI 2010	1" x 1"
SDCv4	C–band SRTM DEM v4 from CGIAR–CSI	Jarvis et al. (2008)	3" x 3" [a]
SDCv2DLR	C–band SRTM DEM v2 from DLR	Wendleder et al. (2016)	3" x 3"
TDX1202	TanDEM–X DEM from February 2012		10 m
TDX1303	TanDEM–X DEM from March 2013		10 m
TDX1311	TanDEM–X DEM from November 2013		10 m
TDX–mosaic	mosaic of stable areas (glacier-free) from TDX1202, TDX1303 and TDX1311		10 m

[a] The 1" x 1" C–band SRTM DEM tiles that are provided by the U.S. Geological Survey were not yet available for the Inylchek Glacier area at the time that the study was conducted.

2.1. TanDEM–X data

We used bistatic TanDEM–X StripMap Horizontal–Horizontal (HH) single polarization CoSSC data for the processing of the TanDEM–X DEMs. The large longitudinal extent of the Inylchek Glacier requires at least two adjacent acquisitions to cover the majority of the glacier body. To minimize discrepancies between the neighbouring DEMs that were used for the mosaicking, we used radar data that were acquired successively with a minimum time difference of 11 days. A total of six TDX acquisitions were computed, which resulted in three mosaicked DEMs with a spatial resolution of 10 m (Tables 1 and 2). The boundaries of all of the data acquisitions are outlined in Fig. 1.

Table 2: Overview of the TanDEM–X acquisitions used to generate the DEMs in this study.

DEM mosaic name	Time	Active satellite	Orbit	Incidence angle (°)	Perpendicular baseline (m)	Multilooking (range×azimuth)
TDX1202	30. Jan 2012	TSX	ascending	36.2	85.6	4×5
	10. Feb 2012	TSX	ascending	38.5	86.6	5×6
TDX1303	01. Mar 2013	TSX	ascending	39.3	117.0	5×6
	12. Mar 2013	TDX	ascending	37.1	112.2	4×5
TDX1311	18. Nov 2013	TDX	descending	33.8	78.7	4×5
	29. Nov 2013	TDX	descending	34.9	77.8	4×5

2.2. External DEMs

Additional DEM data are useful for TDX data-based glacier analysis in two main ways: the DEM can be used to facilitate topographic phase modelling during generation of the interferogram, and it can be used in the actual elevation change comparison. In this study, we refer to the SRTM DEM data as an external source. However, because multiple SRTM DEM versions exist, a careful consideration of an appropriate DEM data set is necessary to achieve optimal results. We initially attempted a direct alignment of our TDX DEMs to the X–band SRTM DEM (hereinafter referred to as SDX; cf. Table 1) provided by the German Aerospace Center (DLR) (©DLR/ASI 2010). This would have been an ideal data set for two reasons: first, Inylchek is almost completely covered

by the SDX data, and seond, the depth of radar penetration will only depend on the snow pack properties at the acquisition time, so complications due to different radar wavelengths could have been neglected. However, this approach is not feasible because the SDX data in our study area show a noisy surface with large elevation discrepancies compared to the C–band SRTM DEM v4 that was provided by CGIAR–CSI (Jarvis et al. (2008); hereinafter referred to as SDCv4; cf. Table 1), which are especially prominent in high elevation areas. After accounting for the height discrepancy between both data sets because of the different vertical datums (EGM96 geoid heights of SDCv4 vs. WGS 84 ellipsoidal heights of SDX), an elevation difference analysis that was performed on off-glacier areas yielded a standard deviation of 77 m.

These significant discrepancies are related to the single or maximum double coverage (in cross sections) of an area with the X–band sensor, whereas the C–band acquisitions were taken from multiple look directions and incident angles, which allowed for better coverage of layover/shadow areas and better smoothing of the resulting DEM (Marschalk et al., 2004). The poor quality of the SDX data in rugged terrain is related to the local incidence angle, slope, aspect and radar beam, whereas errors in the SDCv4 data occurred in areas of original voids and regions with steep slopes (Ludwig and Schneider, 2006; Kolecka and Kozak, 2014). When attempting to use the SDX data as input for topographic phase removal to create differential TanDEM–X interferograms, our results were not as satisfactory as those from the topographic phase removal using SDCv4 data. We therefore concluded that the SDX data are not sufficiently accurate for direct DEM comparisons in our study area, and we used them only for radar-penetration depth correction.

As a result, we aligned our TDX DEMs to the SDCv4. We preferred this void-filled C–band SRTM DEM version to a version that contained voids because it improves the topography removal that is necessary to create a differential interferogram. However, areas that originally contained voids were disregarded for the final elevation change analysis.

As recommended by Nuth and Kääb (2011), we attempted to register the

SDCv4 to data generated by the Geoscience Laser Altimeter System, which is mounted on the Ice, Cloud and Land Elevation Satellite (ICESat) to enable reference consistency for future glacier elevation analyses. We found three stripes of the ICESat GLA14 data that cover the Inylchek area (Zwally et al., 2014), but were challenged when trying to align the data properly. First, 60% of the 9687 original points had to be neglected, because they fall on glaciated areas, which had changed between 2003 and 2009 acquisitions. Second, the terrain surrounding the Inylchek is characterized by steep slopes, which leads to a substantial increase of the standard deviation of the ICESat elevation heights with respect to the SDCv4 heights (Carabajal and Harding, 2006). We therefore excluded points located on slopes steeper than 30°. Rejecting additional outliers that differed by more than ±50 m from the SDCv4 data left us with a sample of 1744 (18%) valid measurements. Because these were mainly located in the northern part of our DEM section, a subsequent alignment attempt yielded unsatisfying results.

Alternatively, we used a version of a C–band SRTM DEM v2 that was computed by DLR (hereinafter referred to as SDCv2DLR; cf. Table 1), in which the correction towards the ICESat data was done on a global scale (Wendleder et al., 2016). This approach ensured a good absolute alignment of the SDCv4 and consequently the TDX DEMs. A drawback of this data set is that it contains many voids, which are generally located in high elevation areas where the SDCv4 data set had been interpolated or filled by additional data sets. Voids also arise from outlier removal and bilinear interpolation during resampling of the data set. As a result, we decided not to use the SDCv2DLR data set for glacier comparison but rather used it as input data to correct the alignment of the SDCv4.

2.3. Glacier outlines of Inylchek

To ensure that the alignments between various data sets are performed only on stable and snow-free areas, we extracted the glacier extents provided by the Randolph Glacier Inventory v3.2 (Arendt et al., 2012; Pfeffer et al., 2014) and

those stored in the Global Land Ice Measurements from Space Inventory (Khromova and Lavrentiev, 2006; Raup et al., 2007). We also used the boundary of the Inylchek Glacier from Shangguan et al. (2015). We manually adjusted this outline in the area of the two glacier tongues to meet the glacier coverage from 2000 by extracting their edges from the SDCv4 DEM. We ultimately combined all three glacier extent data sets to generate a boundary of the maximum potentially glaciated area in the study region. The outline of the Inylchek Glacier from Shangguan et al. (2015) was also used to perform elevation difference measurements.

3. Methodology

This section describes the generation of the TDX DEMs. We first focus on the interferometric processing chain, where we describe the parameters and discuss processing caveats. We then cover the DEM alignment procedure that must be undertaken to allow precise elevation comparison, followed by the handling of radar signal penetration into snow and ice. Finally, we summarize the accuracy assessment.

3.1. Interferometric processing of TanDEM–X data

To derive the DEMs, we applied single-pass Interferometric Synthetic Aperture Radar (InSAR) to the TDX CoSSC data (Graham, 1974; Hanssen, 2001) using the GAMMA software (Werner et al., 2001). Multilook values were chosen to achieve a spatial resolution of 10 m (Table 2). Coregistering was neglected because the TDX pairs were already aligned to each other. Topography removal was done by applying the spatially resampled SDCv4 data. The differential interferograms were filtered with an adaptive filter (Goldstein and Werner, 1998) with a window size of 8 pixels, a window step size of 1 pixel and an alpha value of 0.4. Because the Inylchek area is very rugged, the coherence was estimated with respect to the slope of the terrain and adaptively alternated based on an initial coherence estimate; the window size that was used for the final calculation

ranged between 7 pixels for low coherence areas and 3 pixels for high coherence areas. For the phase unwrapping, we applied the branch-cut method (Rosen et al., 1994) with a maximum branch length of 25 pixels. In contrast to minimum cost flow methods, this minimized the introduction of phase-jumps within connected areas. A caveat of this method was that remaining data gaps due to unconnected regions or low coherence values could not be resolved. These gaps were especially prominent in the high elevation mountain range between the two glacier branches. However, our main goal was to avoid introducing errors over the glaciated regions during the phase unwrapping. We thus accepted data gaps on the steep unglaciated slopes of the mountains rather than trying to resolve as many pixels as possible.

The postprocessing of the unwrapped differential interferogram consisted of several steps. First, the remaining phase jumps were removed by either manual correction (adding multiples of $\pm 2\pi$) or masking, and, missing linked areas were connected to the main interferogram where possible (Fig. 2). We then applied a 2D quadratic phase model to deramp our results. However, this approach was not able to entirely remove an overall ramp, and we corrected for this with a tilt-removal during the DEM alignment. After re-applying the topographic phase to the differential interferogram, we refined our DEMs by applying outlier removal, small data gap interpolation, and spatial smoothing. The outlier removal was achieved as follows. Initially, we smoothed each generated TDX DEM with a 5×5 pixel kernel. We then subtracted the result from the non-smoothed TDX DEM version and calculated the standard deviation σ of the resulting difference image without considering extrapolated values that were introduced during the smoothing procedure. Values outside the 2σ range were masked out. Next, we interpolated only very small data gaps to avoid excessive extrapolation into larger data gaps (a 'no data' pixel must have at least one valid neighbour). In the last refinement step, the DEM was smoothed using a 3×3 boxcar filter, again by avoiding extrapolation. Finally, the individual DEMs were geocoded to the WGS 84 system and projected to UTM coordinates with a spatial resolution of 10 m.

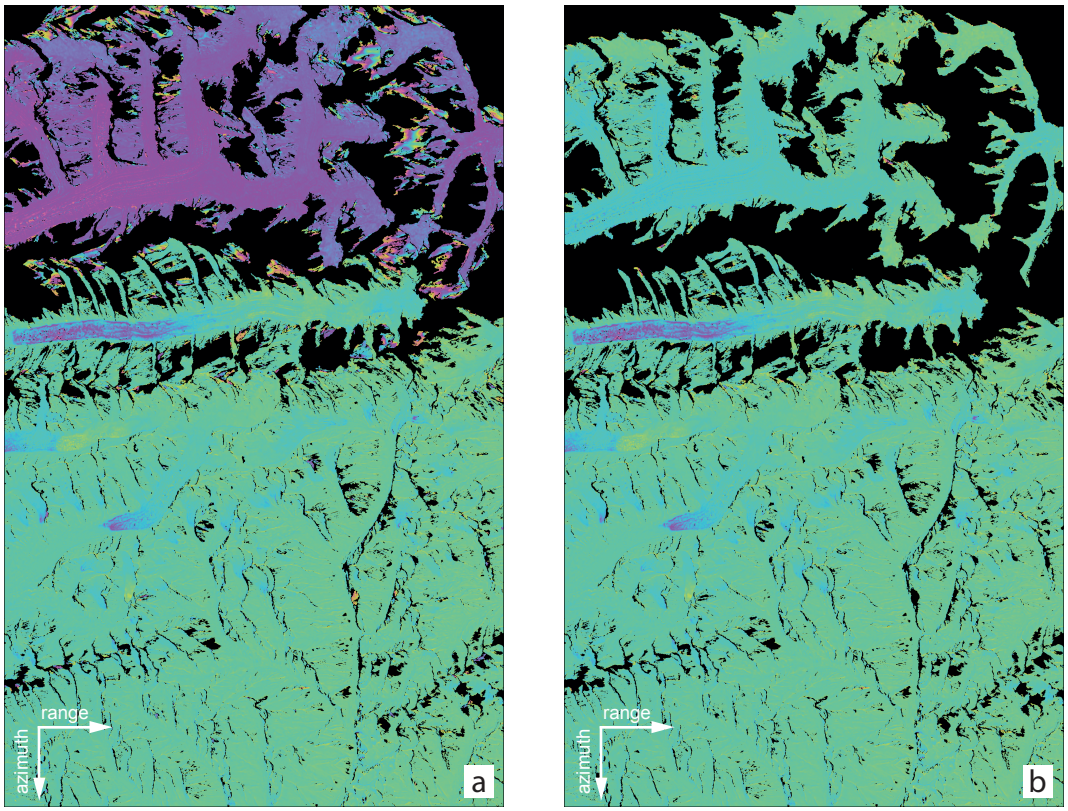

Figure 2: Example unwrapped differential TDX interferogram from 01. March 2013 before (a) and after (b) manual editing, in which the upper part of the differential interferogram was corrected by adding 4π to the phase. Both figures use the same colour cycle scaling.

Each adjacent TDX DEM pair was mosaicked together. Because small tilts persisted in the generated TDX DEMs, we detrended the data pairs relative to each other before mosaicking them by calculating a linear plane fit between the overlapping area of each master and slave DEM, which was then used to correct the entire slave DEM. We mosaicked the two data pairs by neglecting small elevation changes that occurred between the two acquisitions (Table 3). If both data sets contained valid information at the same pixel location we took the mean if they did not differ by more than 10 m, otherwise the pixel was set to 'no data'.

Table 3: Elevation differences of overlapping areas (including snow and ice) and those of the Inylchek Glacier only from the corresponding two TanDEM–X pairs after detrending and removal of differences greater than 10 m.

DEM	Entire overlapping area		Inylchek Glacier only	
mosaic name	Mean (m)	Std. Dev. (m)	Mean (m)	Std. Dev. (m)
TDX1202	-0.002	2.05	-0.02	1.47
TDX1303	0.05	1.95	0.01	1.36
TDX1311	0.001	1.99	-0.11	1.48

3.2. Alignment of the SRTM and TDX DEMs

Before the evaluation of the glacier elevation change can be carried out, all of the available DEMs need to be carefully aligned to each other. This requires all of the data sets to be resampled to the same spatial resolution. Because our main goal is to compare glacier elevation changes between the high-resolution TDX DEMs, we decided to fit the SDCv2DLR and SDCv4 DEMs to the TDX resolution and resampled them to 10 m. The calculation of the alignment parameters is performed on the masked versions of the DEMs, where all of the pixels on unstable terrain were removed to prevent the influence of varying glacier heights on the matching process. The determined alignment parameters are then directly applied to the complete DEMs that contain glacier areas. Additionally, one large glacier-free TDX DEM (hereinafter referred to as TDX–mosaic) was created by merging the stable areas of all three individual TDX DEMs (TDX1202, TDX1303, TDX1311). This product was used to align the TDX DEMs to the SRTM DEM data. Below, we describe the data alignment process in detail. The connections between the individual datasets are shown in Fig. 3.

As recommended in the overview study of Paul et al. (2015), we relied on the approach described by Nuth and Kääb (2011) to properly align the DEMs. Their so-called universal coregistration is based on the dependence of the biases of the slope, aspect and elevation difference. We slightly modified the coregis-

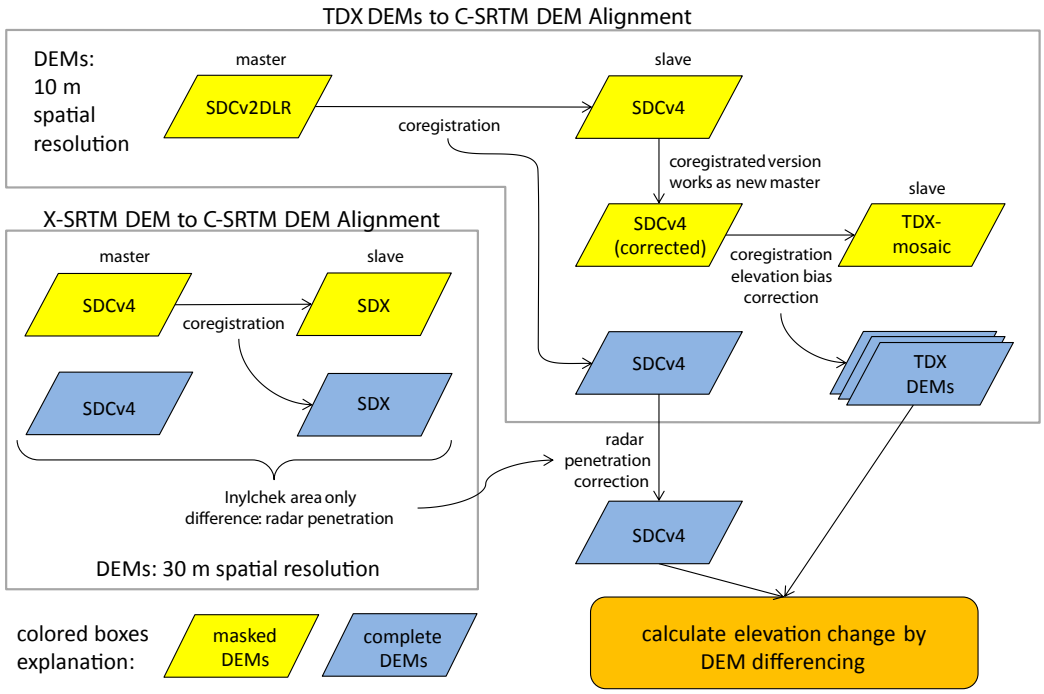

Figure 3: Overview of the alignment process of the DEMs and their respective links. The coregistration and elevation bias parameters are always calculated on masked DEMs that contain only the stable areas (yellow boxes). The retrieved parameters are then used to correct the complete DEMs (blue boxes). The elevation differences retrieved from the subtraction of SDCv4 from SDX are used as inputs to correct the radar penetration offset of the coregistered SDCv4. After all of the corrections were applied, the elevation change calculations were performed.

tration procedure; the estimations of the direction and magnitude of the shift vector were performed as described by the authors, but we did not follow their suggestion to derive the overall vertical bias by dividing the mean bias by the mean slope tangent of the terrain. Instead, we calculated the vertical offset Δz in a separate step by applying a least-squares adjustment with the following function:

$$\Delta z = a + bx + cy, \tag{1}$$

where x and y are the range and azimuth directions, respectively. By either estimating all three parameters (a, b and c) or setting b and c to zero, we controlled for the tilt correction between the DEMs. We refer to this step as DEM detrending.

Our approach also differs from Nuth and Kääb (2011) in that we started the iteration process with DEM detrending and thus first applied a vertical shift and then calculated the horizontal shift parameters from the universal coregistration. This change of the order of the processing steps facilitates improved horizontal matching because DEM detrending includes the removal of possibly existing tilts. If the result did not satisfy the defined threshold parameters, we repeated the detrending and registration procedures iteratively until a predefined threshold criterion was met. The final horizontal shift vector was then calculated by summing all of the individual horizontal shifts that were performed during the iteration and applying the sum to the initial slave DEM. We then applied the DEM detrending step once to this horizontally corrected slave DEM to obtain the best vertical fit as well.

During the DEM alignment, we constrained the fitting procedure as follows. DEM detrending was performed by applying weights w that depended on the corresponding slope α to each elevation difference pixel: $w = (90.0° - \alpha)/90.0°$. Detrending of the SDX data set benefited from a restriction of the fitting process to slopes less than 10°. For all alignment processes that involved TDX scenes, we additionally allowed for a plane tilt removal. Table 4 gives an overview of the applied constrains for the individual DEM pairs.

The parameter calculation of the universal coregistration was based on the median values of each terrain aspect bin, which minimized the influence of outliers (boxplots of the first iteration results are given in Fig. 4). We also considered only slopes greater than 10° because only these elevation differences are meaningful. Pixels with elevation differences greater than 300 m were removed from the statistical analysis (Kääb, 2005). In general, the iterations continued until either the change of the magnitude of the shift vector was less than 0.2 m or the improvement of the standard deviation was less than or equal to 1%.

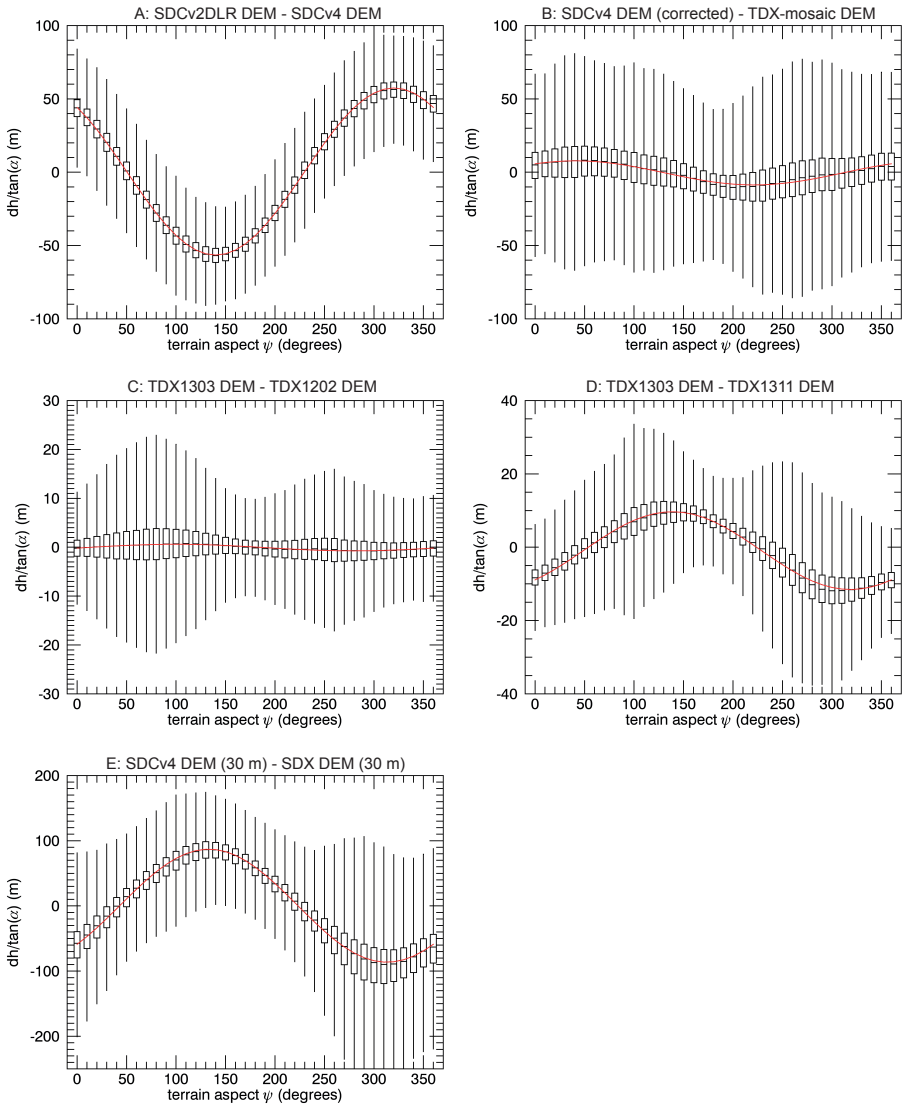

Figure 4: Results of the first iteration of the horizontal shift calculation after Nuth and Kääb (2011) showing the significant offsets between the available DEMs, which makes proper DEM alignment inevitable. The aligned glacier-free DEM versions are given in the titles of each plot, in which the master DEM is presented first and the slave DEM is presented second. The red line shows the corresponding fitting function. Note the different scales on the y-axis.

Table 4: Overview of the parameters applied to the DEM pairs during DEM alignment, where x and - indicate whether a constraint was applied or not. The parameters weighted slopes ($w = (90.0° - \alpha)/90.0°$), slope restriction ($\alpha < 10°$) and plane tilt refer to the DEM detrending step (vertical offset calculation). Except for the last DEM alignment, all off the data sets were resampled to a spatial resolution of 10 m.

Aligned DEMs (Master-Slave)	Weighted Slopes	Restricted Slope	Tilting allowed	Elevation bias correction
SDCv2DLR - SDCv4	x	-	-	-
SDCv4 (corrected) - TDX–mosaic	x	-	x	x
TDX1303 - TDX1202	x	-	x	-
TDX1303 - TDX1311	x	-	x	-
SDCv4 (30 m) - SDX (30 m)	x	x	-	-

To account for errors that might have been introduced due to resampling of the SRTM data (Paul, 2008; Gardelle et al., 2012a), we applied an elevation bias correction after the alignment of the TDX–DEMs to the SDCv4. Because the elevation differences at high elevations vary significantly, we did not apply a polynomial function as proposed in Nuth and Kääb (2011) but rather used median differences calculated from 100 m bins directly for the correction.

3.3. Radar penetration correction

Because X–band and C–band radar data are compared to each other, compensation of the signals for the different radar penetration depths is required for snow, ice and firn regions (Rignot et al., 2001; Gardelle et al., 2012a,b; Kääb et al., 2012). In our case, the radar penetration depth refers to the phase centre depth of the interferometric signal.

We estimated the difference by examining the SDX and SDCv4 (bilinearly resampled to 30 m spatial resolution) data. Because both data sets were acquired at the same time, elevation differences over the glacier area should only exist due to the different penetration characteristics of the X–band and C–band sensors. The elevation differences were thus calculated by considering only the Inylchek glacial area and evaluating the height variations of each 100 m elevation

bin. The resulting elevation-dependent radar penetration variances were then applied to the SDCv4 data to enable a direct comparison with the TDX DEM glacier surface elevations. We note that this approach will only provide an approximation of the true radar penetration difference; discrepancies will persist due to different snow cover depths and characteristics between 2000, 2012 and 2013. Additionally, the incidence angle of the radar look direction and the orbit pass affect the radar penetration depth. Nevertheless, the derivation of different glacier surface heights from SDX and SDCv4 is still reasonable because most of the data sets were acquired during the winter; thus, similar conditions can be assumed.

Because the penetration difference should not exceed 10 m (Rignot et al., 2001; Gardelle et al., 2012a), we defined all of the difference values greater than ± 12 m as outliers and did not consider them for the penetration estimation. We thereby prevented erroneous X–band SRTM elevation values from affecting our results. The median values of each elevation bin were used to correct the 10 m resolution resampled SDCv4 but only for areas with elevations below 6000 m a.s.l. At higher elevations, not enough pixels per elevation bin were available to generate reliable results. Instead, we calculated the mean of the correction values applied to the elevations between 5000 and 6000 m a.s.l. and used this value to correct areas with elevations above 6000 m a.s.l.

Figure 5 shows the median penetration differences as a function of elevation. The values range from -1.51 m (3700 m a.s.l.) to 2.98 m (5900 m a.s.l.). As expected, the radar penetration differences between the SRTM DEMs increase with increasing elevation; in lower regions, the glacier is highly covered by debris with little snow cover. Larger snowpacks are only present at the higher elevations. Interestingly, some of the lower elevation bins show negative correction values. This is reasonable when we consider that the stable areas were also partly covered with snow, especially during the winter. During the vertical matching of the SDCv4 DEM and the SDX DEM, the radar penetration difference due to this snow cover was removed. For debris-covered, low-elevation bins with less snow cover than the stable areas, this will result in negative radar

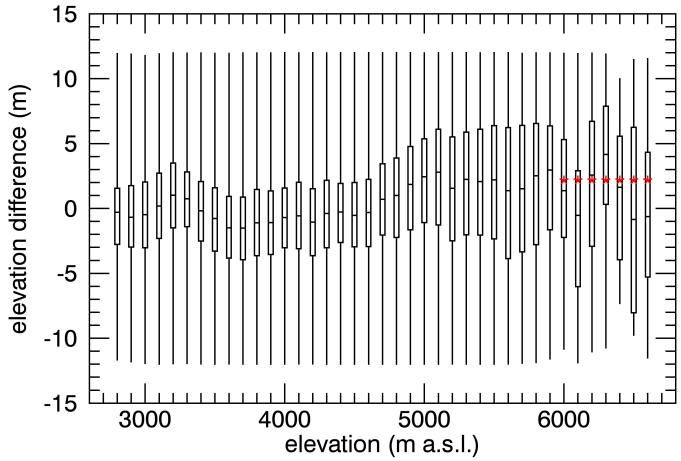

Figure 5: Estimation of radar penetration values for the Inylchek region in 100 m elevation bins retrieved by subtracting SDCv4 from SDX. The boxes show the median values along with the lower and upper quartiles. Whiskers refer to the sample minimum and maximum, respectively. Note that the data range is constrained to a 12 m elevation difference. Elevation differences for elevations above 6000 m were taken from the mean penetration between 5000 and 5900 m (red asterisks) because the small number of pixels does not allow reliable penetration values to be retrieved. The overall uncertainty of the radar penetration is 1.39 m, which was derived from the standard deviation of the medians for all elevation bins below 6000 m a.s.l.

penetration differences.

To estimate the uncertainty of the radar penetration, we calculated the standard deviation of the medians for all elevation bins below 6000 m a.s.l. and determined a value of 1.39 m, which we considered in the accuracy assessment for all direct comparisons between the SDCv4 and TDX DEM data.

3.4. DEM elevation difference calculation

We calculated the elevation difference between each DEM pair based on the area-weighted mean difference for each 100 m elevation bin. Before retrieving the average value, we set pixels that differed by more than 3σ from the mean of each elevation bin to 'no data' (Gardner et al., 2012; Gardelle et al., 2013). We also neglected all interpolated pixels of the SDCv4 DEM data set (Kääb et al., 2012; Gardelle et al., 2013).

Next, all of the 'no data' pixels located within the glacier boundary needed to be addressed carefully before any DEM comparison was undertaken; otherwise, the final results will show under- or overestimated values. Gardelle et al. (2013) proposed using the average of the corresponding elevation bin to fill data gaps. However, we argue that the strong dependency of accumulation/ablation on the hillslope angle of the mountainous areas cannot be neglected. Figure 6 shows the clear dependence of the elevation change on the slopes of the terrain. Areas with lower hillslope angles are more susceptible to elevation changes, and the elevations of steeper areas are affected less. We claim that at a certain slope, the glacier elevation change can be assumed to be stable. This hypothesis is supported by the fact that above 50° hillslope angle, snow tends to slide off regularly (Keller and DeVecchio, 2016). Furthermore, snow nourishing glaciers on lower slopes than 50° may be transported through avalanches, which occur mainly on slopes between 35 and 40° (Keller and DeVecchio, 2016).

As a result, to fill the 'no data' areas, we distinguished between slopes less than and greater than 45°. For the entire glacier region, we set the elevation change of the pixels located in areas with slopes greater than 45° to zero. This had the following two effects. First, many of the data gaps were filled with zero values because most of the data gaps were in high elevation areas with steep slopes, where the TDX radar signal could not be resolved. Second, we reduced the introduction of erroneous values that might occur when a TDX DEM is subtracted from the SDCv4. These errors may be introduced due to the different resolution of the original data. Despite the applied elevation-dependent correction, the SDCv4 elevation values at high elevations can still be underestimated (Berthier et al., 2006; Paul and Haeberli, 2008; Gardelle et al., 2012a), which in turn leads to an underestimation of the calculated volume loss.

In the next step, regions with slope angles of less than 45° were treated as follows to take into account the dependency of the elevation change on the hillslope angle. Data within one elevation bin were separated into three slope classes: 0–15°, 15–30° and 30–45°. Missing pixels were then filled with the mean elevation change values of the corresponding elevation bin and slope class if at

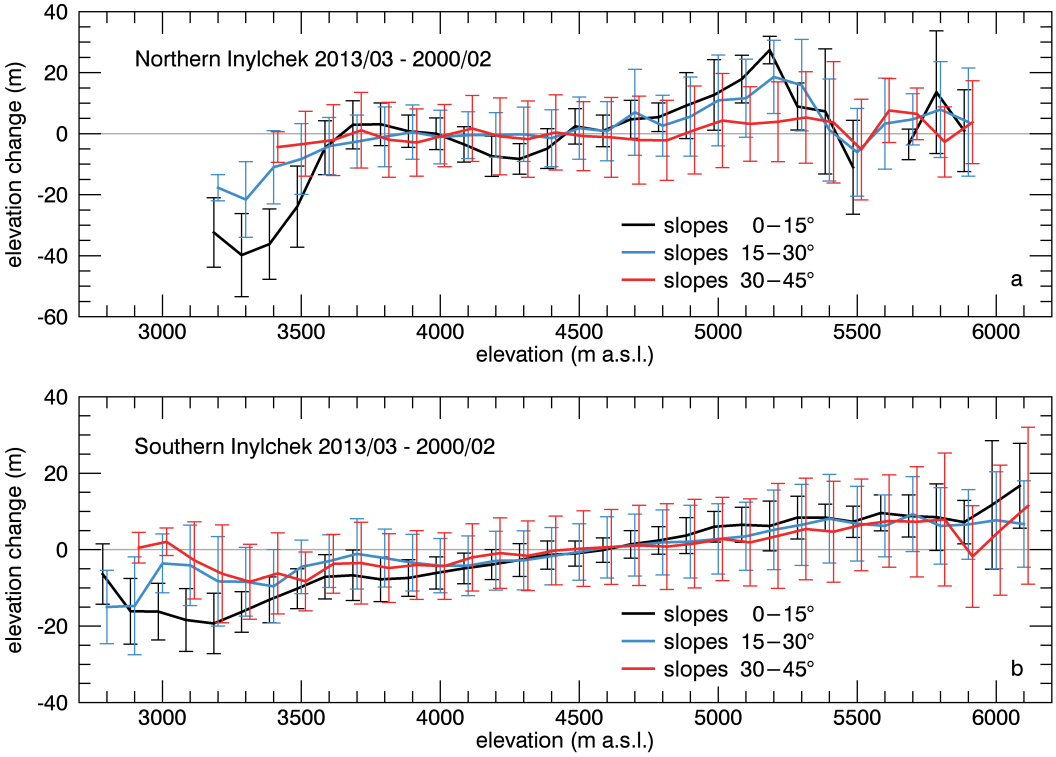

Figure 6: Example elevation changes from the (a) Northern Inylchek and (b) Southern Inylchek glaciers (showing mean and standard deviation values) between February 2000 (SDCv4 DEM) and March 2013 (TDX1303 DEM) as a function of elevation while separating terrain slope angles. The greatest elevation changes occur in small hillslope areas, while glacier regions with steeper slopes are affected less.

least 1% of the valid pixels were available to derive the mean value from. The lowest elevations where this condition did not hold were at 5300 m a.s.l. and 5600 m a.s.l. for Northern and Southern Inylchek, respectively. These elevations were well above the ELA and thus were in the accumulation region. As a result, we filled the remaining missing pixels by following the approach of Pieczonka et al. (2013), who argued that the long-term change in accumulation areas is rather small, so missing pixels in accumulation areas can be assigned to zero. Although our approach already considers several boundary conditions, we emphasize that the mean values derived for the individual classes must be evaluated

carefully to avoid outlier extrapolation. A standard deviation of more than 20 m within a single class was used as a threshold to find existing unrealistic mean values, which were then eliminated from the extrapolation.

The overall elevation change ΔH was calculated as follows (Shangguan et al., 2015):

$$\Delta H = \frac{\sum_{i=1}^{n} \Delta h_i a_i}{A}, \tag{2}$$

where i is the number of elevation bins, Δh_i is the mean elevation difference for the individual elevation bin, a_i is the area of the valid pixels per elevation bin, and A is the total area of all of the elevation bins.

Special attention had to be paid to the calculation of the annual elevation change of the DEM pair for February 2000 to November 2013 because the data were not acquired during the same season. In this case, the seasonal snow height effects will bias the calculation, so we refrained from calculating an annual elevation change rate.

3.5. Accuracy assessment

Several methods have been used to assess the elevation difference uncertainty $u_{DEM1-DEM2}$ between two DEMs, examples are found in studies from Gardelle et al. (2013); Pieczonka et al. (2013); Pieczonka and Bolch (2015) and Shangguan et al. (2015). Similar to the two latter studies, we used an approach that is robust to outliers in which $u_{DEM1-DEM2}$ was derived from the error of the DEM coregistration, which was estimated from the normalized median absolute deviation $\Delta\sigma$ (NMAD) of stable areas (Table 5). Because $\Delta\sigma$ is proportional to the median of the absolute differences between the DEM errors Δh_j ($j = 1, ..., n$, where n is the total number of pixels in stable areas) and the median of these DEM errors $m_{\Delta h_j}$, it can be regarded as an outlier-resilient estimate of the standard deviation (Höhle and Höhle, 2009).

$$\Delta\sigma = 1.4826 \cdot median_j(|\Delta h_j - m_{\Delta h_j}|). \tag{3}$$

For elevation difference calculations between TDX DEMs, we assumed the same radar penetration depth; thus, $u_{TDX1-TDX2}$ denoted as:

$$u_{TDX1-TDX2} = \Delta\sigma \tag{4}$$

However, for the elevation differences $u_{SRTM-TDX}$ that were calculated between the SRTM and TDX DEM data, the accuracy of the radar wave penetration depth Δrw of ± 1.39 m must also be included in the uncertainty estimation:

$$u_{SRTM-TDX} = \sqrt{(\Delta\sigma)^2 + (\Delta rw)^2}. \tag{5}$$

Table 5: Statistics for stable (outside glacier) difference areas. The values between the TDX DEMs were calculated before mosaicking the three stable areas together. NMAD ($\Delta\sigma$) is the normalized median absolute deviation (see text for further explanation).

DEM pair	Mean (m)	Median (m)	Std. Dev. (m)	NMAD (m)
SDCv4 (corrected) - TDX–mosaic	-0.19	0.03	8.07	5.04
TDX1202 - TDX1303	-0.005	-0.001	1.72	1.13
TDX1303 - TDX1311	-0.03	-0.03	2.26	1.13
TDX1202 - TDX1311	0.1	0.09	2.15	1.28

4. Results and discussion

4.1. Uncertainty of measurements

The largest uncertainty in our analysis arises from the significant number of missing values within the DEMs. Quantifying the impact of the filling is difficult. Because we do not take into account any reference data, we can only make assumptions about the void areas. Pieczonka and Bolch (2015) relied on ordinary kriging to fill voids. In our setting, the largest areas of missing data are at high elevations. Applying a kriging method in this case would lead to over-extrapolation, which impairs the filling, as was noted by Pieczonka and Bolch (2015). Filling all data gaps within the accumulation area with zero values may be a valid option for long-term studies because the assumption of

low elevation changes for that region may be true (Pieczonka et al., 2013). However, that does not account for the inter-annual investigations in our study, where changes between consecutive years might be large. We therefore extended the approach of Gardelle et al. (2013) to fill data voids with mean elevation bin values by considering the slope-dependency of the elevation change. Due to side-looking induced geometric distortions of the radar image, most voids occur on the steeper slopes, and thus affect the edges and the higher elevations of high mountain glaciers. Because these glacier areas are affected by glacier changes differently than those on the gentler slopes (Fig. 6), using mean values generated from valid pixels located on these gentler slopes would lead to an overestimation of the glacier change. As a result, mean values from specific slope bins help to improve the glacier elevation change estimates. Still, the amount and width of the useful slope bins must be carefully evaluated by considering the availability of the data. Too many slope classes may result in too few valid pixels within a slope bin, and calculating mean values will become random or even impossible. For the Inylchek Glacier test site, three slope bins between 0° and 45° proved useful. As a result, we assign zero values only to pixels at high elevations with slopes greater than 45° and to areas with slopes between 0° and 45° where no valid information exists to retrieve the mean values from. We tested the impact of the latter method by assigning values of either $\pm\,1\,\mathrm{m}$ instead of zero. The elevation changes revealed maximum absolute elevation change differences of $\pm\,0.04\,\mathrm{m\,a^{-1}}$ (9%) and $\pm\,0.07\,\mathrm{m\,a^{-1}}$ (26%) for Northern and Southern Inylchek, respectively.

An additional uncertainty factor is the estimation of the different radar penetration depths of the X–band and C–band signals into snow and ice. Shangguan et al. (2015) reported greater penetration differences (1.7 m for debris free-area ablation areas and 2.1–4.3 m for elevations between 4000 and 5100 m. a.s.l.) over the Inylchek area than our investigation. However, these authors did not apply any DEM alignment between the X–band SRTM DEM and the C–band SRTM DEM in advance, and we used a strict outlier removal strategy ($\pm 12\,\mathrm{m}$), which might explain the differences.

Kääb et al. (2012) provides C–band radar wave penetration estimates for various mountainous regions of Asia that were derived by a differentiation of C–band SRTM DEM elevation to ICESat elevations. A direct comparison between their values and ours is only partially possible because we did not correct for a discrepancy that is generated by the penetration of X–band SAR into snow and ice. However, we expect that this discrepancy will play only a minor role in ice-dominated debris-free ablation regions but has a greater impact in the snow/firn-dominated areas of the accumulation region. Taking this into consideration, our penetration estimates are consistent with the values given by Kääb et al. (2012), which include 2.5 ± 0.5 m over general glacier areas, -0.8 ± 1.0 m over debris-covered ice, 0.1 ± 1.2 m over clean ice and 4.8 ± 0.7 m over the firn/snow areas of the glaciers in the East Nepal and Bhutan mountain range that, similar to Inylchek, are summer-accumulation type glaciers (Kääb et al., 2012).

It is worth noting that due to the short time period of this investigation, the uncertainties between the TDX DEMs are greater than average compared to similar studies that consider optical data such as KH–9 Hexagon and SPOT–5 data. However, we emphasize that low mass balance uncertainties of $0.10\,\mathrm{m\,a^{-1}}$ between KH–9 and SRTM data or $0.11\,\mathrm{m\,a^{-1}}$ between KH–9 and SPOT–5 data (Shangguan et al., 2015) can be only achieved when looking at long time spans (in their case, 24 years and more), whereas the same accuracy is theoretically achieved from TDX comparisons with an acquisition difference of nine years.

4.2. DEM alignment quality

The evaluation of elevation differences within stable areas between two DEMs gives insights on the quality of the DEM alignment. In our case, the comparison between the SDCv4 and TDX data yields an absolute mean elevation difference of approximately 0.2 m with a standard deviation of 8 m (Table 5). These discrepancies are mainly attributed to the different spatial resolutions of the DEMs. The high potential of the TDX DEM data for the analysis of glacier changes is demonstrated by the comparison of only the TDX DEMs. Here, the elevation differences are in the range of a few centimetres with corresponding standard

deviation values of 2 m, which is at least two times smaller than when comparing TDX DEMs to SDCv4 data. The best agreement is achieved between the two TDX DEMs that are taken from the same orbit and incidence angle (TDX1202–TDX1303: -0.005 ± 1.72 m), but the differences with TDX1311, which had the opposite orbit, are only slightly larger (TDX1303–TDX1311: -0.03 ± 2.26 m and TDX1202–TDX1311: 0.1 ± 2.15 m; cf. Table 5). However, these variations may be attributed to orbital discrepancies or processing errors as well as the different seasons of the data collection. Because snowfall over stable areas cannot be excluded, the characteristics and depth of the snow may differ on the dates of the data collection, which results in different penetration effects and ultimately in different elevation changes.

Although all TDX DEM comparisons are characterized by large absolute uncertainties compared to the corresponding elevation changes, the good quality of the DEMs is also demonstrated by the high internal consistency between the three TDX DEM pairs. The difference between the sums of the absolute glacier elevation changes of TDX1202–TDX1303 and TDX1303–TDX1311 is only 7 cm for the Northern Inylchek branch and 3 cm for the Southern Inylchek branch compared to the corresponding differences retrieved from the DEM pair that covers the time period TDX1202–TDX1311 (Table 6). The superior accuracy of the TDX DEMs compared to SDCv4 is also confirmed by the 4–5 times lower absolute elevation change uncertainty values of the direct TDX DEM comparisons.

4.3. Inylchek elevation changes

As shown in Table 6 and Fig. 7, both branches of the Inylchek Glacier have been affected by thinning since 2000, and the northern branch has experienced higher downwasting rates than the southern branch. Mapping the elevation changes shows the spatial distribution of areas of elevation loss and gain. The ablation area of Northern Inylchek is most severely affected by glacier loss with rates up to 60–70 m over 13 years, whereas the accumulation areas of both branches show slight gains of between 1 and 10 m since 2000 (Fig. 8). The

Table 6: Elevation changes of the Southern and Northern Inylchek glacier branches.

(a) Northern Inylchek (159 km^2)

DEM pair	absolut elevation change (m)	elevation change per year (m a^{-1})
SDCv4 - TDX1202	-2.88 ± 5.23	-0.24 ± 0.44
SDCv4 - TDX1303	-3.68 ± 5.23	-0.28 ± 0.40
SDCv4 - TDX1311	-3.22 ± 5.23	-
TDX1202 - TDX1303	-0.34 ± 1.13	-0.32 ± 1.04
TDX1303 - TDX1311	-0.57 ± 1.13	-
TDX1202 - TDX1311	-0.84 ± 1.28	-

(b) Southern Inylchek (508 km^2)

DEM pair	absolut elevation change (m)	elevation change per year (m a^{-1})
SDCv4 - TDX1202	-1.69 ± 5.23	-0.14 ± 0.44
SDCv4 - TDX1303	-1.98 ± 5.23	-0.15 ± 0.40
SDCv4 - TDX1311	-1.76 ± 5.23	-
TDX1202 - TDX1303	-0.42 ± 1.13	-0.38 ± 1.04
TDX1303 - TDX1311	-0.27 ± 1.13	-
TDX1202 - TDX1311	-0.72 ± 1.28	-

high spatial resolution of the TDX data also allows precise mapping of the inter- and intra-annual elevation changes (Fig. 9), which offer a unique view on the underlying glacial processes. For example, an increase in surface elevation occurred in the middle part of the northern branch during 02/2012–03/2013 (Fig. 9b), and a distinct elevation loss occurred at an icefall on the main southern tributary of Southern Inylchek during 03/2013–11/2013 (Fig. 9c). We emphasize that changes at these short timescales cannot be observed from the annual mean elevation change shown in Fig. 9a. Retrieving DEMs from TDX data is therefore especially helpful for investigating inter- and intra-annual time scales.

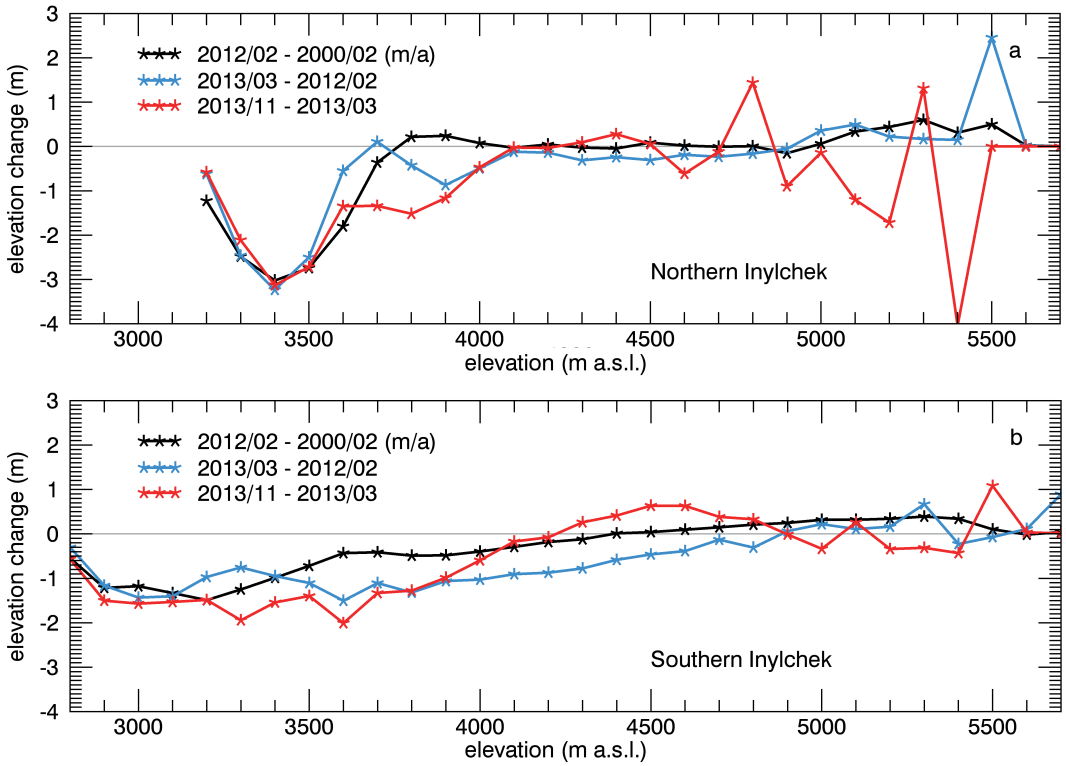

Figure 7: Elevation changes of a) Northern Inylchek and b) Southern Inylchek as a function of elevation. The data represent mean changes per 100 m elevation bin (marked with asterisks).

Pieczonka and Bolch (2015) and Shangguan et al. (2015) used optical remote sensing imagery to analyse mass balance rates of the Inylchek Glacier. Both studies showed that within the time period 1975–1999 mass loss rates over the Southern Inylchek glacier branch were higher (-0.27 ± 0.45 m w.e.a^{-1} in Pieczonka and Bolch (2015) and -0.43 ± 0.10 m w.e.a^{-1} in Shangguan et al. (2015)) than those over the Northern Inylchek glacier branch (-0.19 ± 0.45 m w.e.a^{-1} in Pieczonka and Bolch (2015) and -0.25 ± 0.10 m w.e.a^{-1} in Shangguan et al. (2015)). However, Shangguan et al. (2015) also investigated mass changes between 1999–2007 and reported an increase of Northern Inylchek's downwasting values to -0.57 ± 0.46 m w.e.a^{-1}, which was higher than Southern Inylchek's mass loss of -0.28 ± 0.46 m w.e.a^{-1} in the same time period.

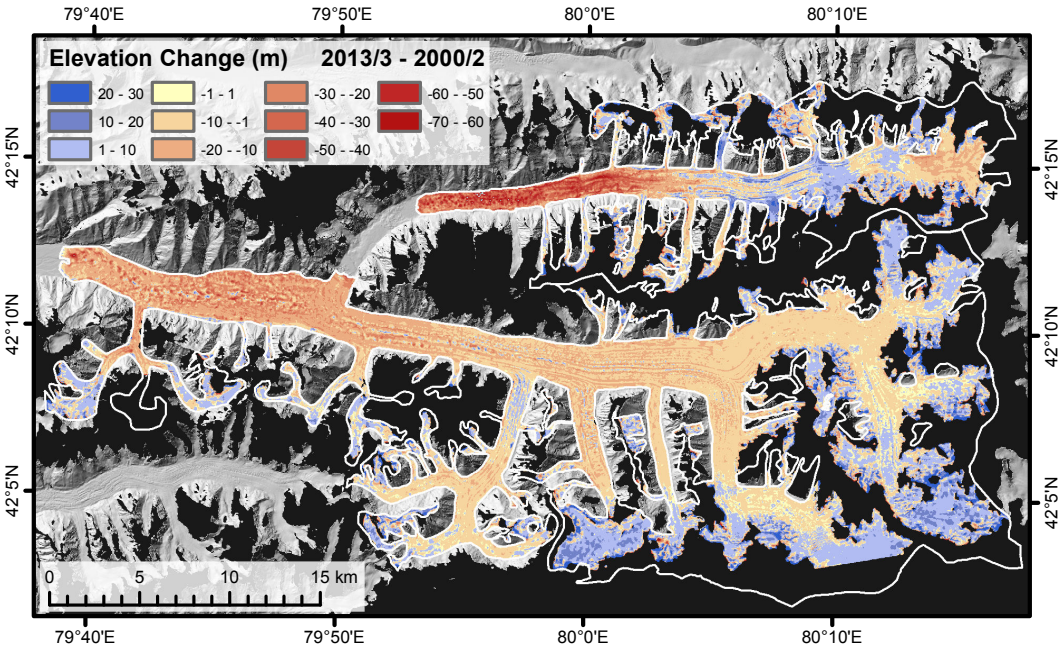

Figure 8: Absolute elevation changes between SDCv4 and TDX1303. The white polygons outline the Inylchek Glacier. Negative values indicate elevation losses (red), and positive values indicate elevation gains (blue).

For comparison purposes, we converted the 02/2000–03/2013 glacier elevation changes of this study to mass balance values by applying the geodetic method. For conversion, we assumed an ice density of $850\,\mathrm{kg\,m^{-3}}$ (Huss, 2013) and used a value of $999.972\,\mathrm{kg\,m^{-3}}$ for the water density. The resulting mass balance is in the order of $-0.24 \pm 0.34\,\mathrm{m\,w.e.a^{-1}}$ for Northern Inylchek and $-0.13 \pm 0.34\,\mathrm{m\,w.e.a^{-1}}$ for Southern Inylchek. Our estimation agrees with Shangguan's findings in such a way that Northern Inylchek is loosing more mass per year than Southern Inylchek. However, our results suggest that this is related rather to a deceleration of Southern Inylchek's downwasting than to a significant increase of the thinning of the Northern Inylchek branch.

As the findings of Shangguan et al. (2015) resulted in significantly higher mass-loss values than our findings further research into this discrepancy is required. A potential explanation is the application of different radar penetra-

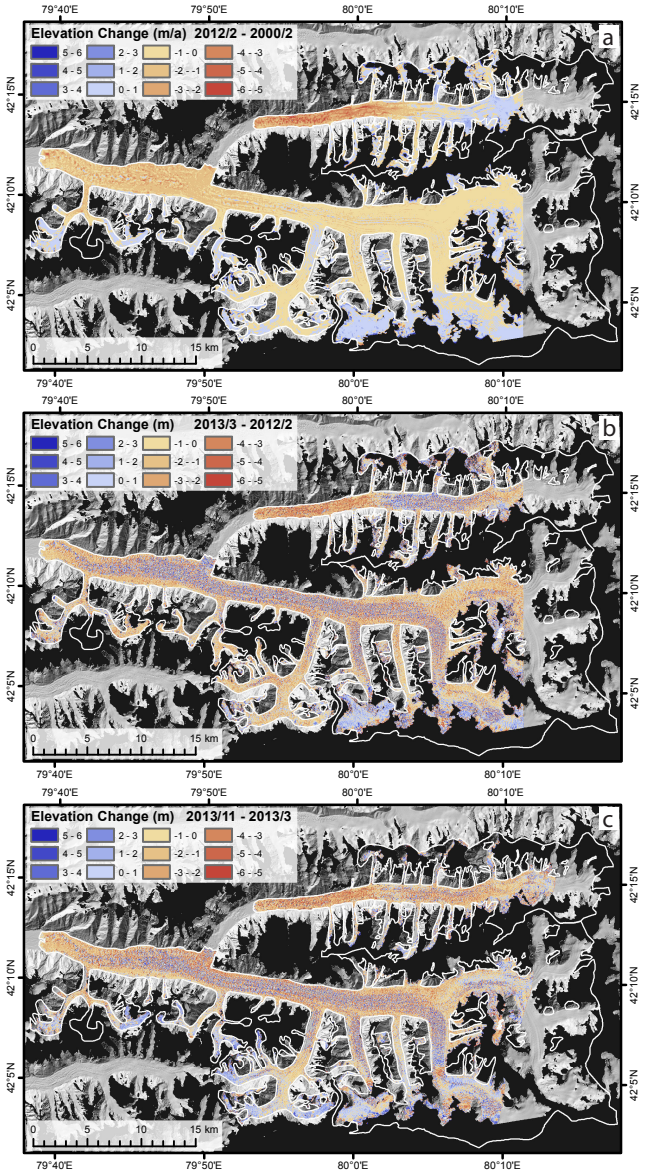

Figure 9: Elevation changes between the SRTM and TanDEM–X acquisitions: a) between SDCv4 and TDX1202 (mean annual change), b) between TDX1202 and TDX1303, and c) between TDX1303 and TDX1311. The white line represents the boundary of the Inylchek Glacier.

tion depth corrections in Shangguan et al. (2015). We tested the impact of the radar penetration depth on the mass balance calculation by increasing it by ± 1 m, which resulted for both glacier branches in a mass balance change of ± 0.06 m w.e.a^{-1}. This refers to a change of $\pm 25\%$ and $\pm 46\%$ w.e.a^{-1} for Northern and Southern Inylchek, respectively. As the discrepancies to Shangguan et al. (2015) are still larger, radar penetration depth is likely not the only influencing factor. Another possible explanation might be the data voids in the accumulation regions in the study of Shangguan et al. (2015). The mass gain that we detected especially in the Southern Inylchek accumulation area was not resolved in their study (cf. to Fig. 4b in Shangguan et al. (2015)).

5. Conclusions

TerraSAR–X and simultaneously recorded TanDEM–X (TDX) radar data are ideal to generate digital elevation models in high mountain areas, where weather conditions often prevent monitoring with optical remote sensing devices. Because of their spatial coverage, they are especially suitable to assess glacier elevation changes for broad areas. However, steep slopes and high relief of mountain areas make generating DEMs from single SAR image pairs a challenging task. We investigated in detail (1) the suitability of SRTM-based reference DEMs to enable long-wavelength topographic phase removal to derive differential interferograms; (2) the impact of interferometric processing parameters on DEM generation (e.g., coherence, unwrapping procedures); (3) the importance of precise DEM alignment; (4) the effect of radar penetration into snow and ice; (5) the filling of data voids in glaciated areas; and (6) the accuracy that can be achieved from using TDX based DEMs. This leads to the following conclusions:

(1) Although X–band SRTM DEM data covers our study almost completely, we use C–band SRTM DEM data for topographic phase modelling because noisy surfaces and inaccuracies at steep slopes in the X–band SRTM DEM hamper the interferogram generation.

(2) Due to the side-looking nature of the sensor, geometric distortions in the

radar data resulting from foreshortening, layover and shadowing effects cannot be avoided. To prevent an erroneous glacier elevation change analysis, it is important to minimize the effects of errors due to phase jumps and low coherence over the glacier area. As a result, we prefer a branch-cut algorithm for phase unwrapping. To ensure that large glacier areas are not lost due to missing connections of separately unwrapped areas, careful evaluation and manual editing of the unwrapped interferogram is required, which makes the automation of DEM generation difficult.

(3) Precise alignment of all DEMs is inevitable for glacier elevation change calculation. We apply a modified version of the universal coregistration procedure introduced by Nuth and Kääb (2011).

(4) Glacier surface elevation differences caused by radar signal penetration into snow and ice must also be considered. This becomes even more important when data that were collected with different wavelengths are compared to each other. We analyse the impact of radar penetration due to wavelength differences by comparing height variations of C–band and X–band SRTM DEMs. The results are used to correct elevation changes estimated from comparing C–band SRTM with TDX DEMs. However, these corrections are only an approximation of the true radar penetration differences because seasonal effects, such as different snow coverage at different acquisition times, also influence the backscatter of the radar signal. These effects cannot easily be corrected for, which makes a precise estimation of the radar penetration a challenging task.

(5) The uncertainties of glacier elevation change estimates generally increase with increased data gaps of the glaciated areas. The closure of these voids should therefore preferably be done by considering additional radar data from either a different orbit or another incidence angle if the data acquisition times are not significantly different. Alternatively, elevation data from complementary optical data or other sources can be considered, but the condition of equal acquisition times is still valid. If no additional data are available, assumptions must be made regarding the glacier elevation changes in the void areas. We suggest that missing values should be derived from values of valid glacier surface areas with

similar surface geometric conditions, particularly similar elevations and slope angles. If no valid data from similar areas are available, assumptions such as zero glacier elevation change in accumulation areas can be applied at the expense of significant higher uncertainties.

(6) We show that careful treatment of all of the uncertainty factors of TDX generated DEM data is required to obtain a precise, quantitative estimate of glacier elevation changes. This is especially important when analysing intra- and inter-annual timescales. Our results show that TDX DEMs are suitable for estimating glacial elevation changes and we highlight the following key results. First, the deviations between the stable areas of all of the TDX DEMs generated here are low (max. 0.1 ± 2.15 m). Second, the TDX DEMs are internally consistent: the sums of the independently calculated glacier elevation changes from 2012/02 to 2013/03 and 2013/03 to 2013/11 differ by only 0.07 m for Northern Inylchek and 0.03 m for Southern Inylchek compared to glacier elevation changes that are calculated directly from the DEM pair from 2012/02–2013/11. Third, the absolute uncertainty of the glacier elevation changes is 1.13 m for the TDX DEM glacier comparisons, which is significantly lower than the 5.23 m for the comparison between the C–band SRTM and TDX DEMs. Our findings demonstrate the high potential of using single-pass TDX DEMs to monitor for glacier development in high mountain areas. The high accuracy and spatial resolution make TDX DEMs especially suitable for investigations of highly dynamic glacier elevation changes ranging from rapid surge events to seasonal-to-decadal changes in response to global changes.

Author contribution

M.M. and J.N. designed the study with support from B.B. J.N. generated the TDX DEMs, adapted the DEM alignment method, determined the glacier elevation changes and prepared the manuscript. M.M. and B.B. contributed to the analysis, discussion and writing.

Acknowledgements

This study was supported by the Initiative and Networking Fund of the Helmholtz Association in the framework of the Helmholtz Alliance "Remote Sensing and Earth System Dynamics" (EDA). The authors thank D. H. Shangguan and T. Bolch for providing the Inylchek Glacier outline and A. Wendleder and A. Roth from the German Aerospace Center (DLR) for distributing the ICESat-corrected C–SRTM DEM. The TanDEM–X (proposal ID XTI_GLAC6883) and SRTM–X DEM data were also kindly provided by DLR. The C–SRTM DEM v4 was derived from the Consortium for Spatial Information of the Consultative Group for International Agricultural Research (CGIAR–CSI). The Landsat data were obtained from the U.S. Geological Survey.

References

Aizen, V. B., Aizen, E. M., Dozier, J., Melack, J. M., Sexton, D. D., and Nesterov, V. N.: Glacial regime of the highest Tien Shan mountain, Pobeda–Khan Tengry massif, Journal of Glaciology, 43, 503–512, 1997.

Aizen, V. B., Aizen, E. M., Joswiak, D. R., Fujita, K., Takeuchi, N., and Nikitin, S. A.: Climatic and atmospheric circulation pattern variability from ice-core isotope/geochemistry records (Altai, Tien Shan and Tibet), Annals of Glaciology, 43, 49–60, doi:10.3189/172756406781812078, 2006.

Aizen, V. B., Aizen, E. M., and Kuzmichonok, V. A.: Glaciers and hydrological changes in the Tien Shan: simulation and prediction, Environmental Research Letters, 2, 045019, doi:10.1088/1748-9326/2/4/045019, 2007.

Arendt, A., Bolch, T., Cogley, J. G., Gardner, A. S., Hagen, J.-O., Hock, R., Kaser, G., Pfeffer, W. T., Moholdt, G., Paul, F., Radić, V., Andreassen, L., Bajracharya, S., Barrand, N., Beedle, M., Berthier, E., Bhambri, R., Bliss, A., Brown, I., Burgess, D., Burgess, E., Cawkwell, F., Chinn, T., Copland, L., Davies, B., De Angelis, H., Dolgova, E., Filbert, K., Forester, R., Fountain, A., Frey, H., Giffen, B., Glasser, N., Gurney, S., Hagg, W., Hall, D., Haritashya, U., Hartmann, G., Helm, C., Herreid, S., Howat, I., Kapustin, G., Khromova, T., Kienholz, C., König, M., Kohler, J., Kriegel, D., Kutuzov, S., Lavrentiev, I., Le Bris, R., Lund, J., Manley, W., Mayer, C., Miles, E., Li, X., Menounos, B., Mercer, A., Mölg, N., Mool, P., Nosenko, G., Negrete, A., Nuth, C., Pettersson, R., Racoviteanu, A., Ranzi, R., Rastner, P., Rau, F., Raup, B., Rich, J., Rott, H., Schneider, C., Seliverstov, Y., Sharp, M., Sigurðsson, O., Stokes, C., Wheate, R., Winsvold, S., Wolken, G., Wyatt, F., and Zheltyhina, N.: Randolph Glacier Inventory – A Dataset of Global Glacier Outlines: Version 3.2., Global Land Ice Measurements from Space, Boulder Colorado, USA. Digital Media, 2012.

Berthier, E., Arnaud, Y., Vincent, C., and Rémy, F.: Biases of SRTM in high-

mountain areas: Implications for the monitoring of glacier volume changes, Geophysical Research Letters, 33, L08502, doi:10.1029/2006GL025862, 2006.

Bevan, S. L., Luckman, A., Khan, S. A., and Murray, T.: Seasonal dynamic thinning at Helheim Glacier, Earth and Planetary Science Letters, 415, 47–53, doi:10.1016/j.epsl.2015.01.031, 2015.

Bhambri, R., Bolch, T., and Chaujar, R. K.: Mapping of debris-covered glaciers in the Garhwal Himalayas using ASTER DEMs and thermal data, International Journal of Remote Sensing, 32, 8095–8119, doi:10.1080/01431161.2010.532821, 2011.

Carabajal, C. C. and Harding, D. J.: SRTM C-Band and ICESat Laser Altimetry Elevation Comparisons as a Function of Tree Cover and Relief, Photogrammetric Engineering & Remote Sensing, 72, 287–298, doi:10.14358/PERS.72.3.287, 2006.

Erten, E., Reigber, A., Hellwich, O., and Prats, P.: Glacier Velocity Monitoring by Maximum Likelihood Texture Tracking, IEEE Transactions on Geoscience and Remote Sensing, 47, 394–405, doi:10.1109/TGRS.2008.2009932, 2009.

Farinotti, D., Longuevergne, L., Moholdt, G., Duethmann, D., Mölg, T., Bolch, T., Vorogushyn, S., and Güntner, A.: Substantial glacier mass loss in the Tien Shan over the past 50 years, Nature Geoscience, 8, 716–722, doi:10.1038/ngeo2513, 2015.

Fischer, A.: Comparison of direct and geodetic mass balances on a multi-annual time scale, The Cryosphere, 5, 107–124, doi:10.5194/tc-5-107-2011, 2011.

Friedt, J.-M., Tolle, F., Bernard, É., Griselin, M., Laffly, D., and Marlin, C.: Assessing the relevance of digital elevation models to evaluate glacier mass balance: application to Austre Lovénbreen (Spitsbergen, 79°N), Polar Record, 48, 2–10, doi:10.1017/S0032247411000465, 2012.

Gardelle, J., Berthier, E., and Arnaud, Y.: Impact of resolution and radar penetration on glacier elevation changes computed from DEM differencing, Journal of Glaciology, 58, 419–422, doi:10.3189/2012JoG11J175, 2012a.

Gardelle, J., Berthier, E., and Arnaud, Y.: Slight mass gain of Karakoram glaciers in the early twenty-first century, Nature Geoscience, 5, 322–325, doi:10.1038/ngeo1450, 2012b.

Gardelle, J., Berthier, E., Arnaud, Y., and Kääb, A.: Region-wide glacier mass balances over the Pamir-Karakoram-Himalaya during 1999–2011, The Cryosphere, 7, 1263–1286, doi:10.5194/tc-7-1263-2013, 2013.

Gardner, A., Moholdt, G., Arendt, A., and Wouters, B.: Accelerated contributions of Canada's Baffin and Bylot Island glaciers to sea level rise over the past half century, The Cryosphere, 6, 1103–1125, doi:10.5194/tc-6-1103-2012, 2012.

Glazirin, G. E.: A century of investigations on outbursts of the ice-dammed lake Merzbacher (central Tien Shan), Austrian Journal of Earth Sciences, 103, 171–179, 2010.

Goldstein, R. M. and Werner, C. L.: Radar interferogram filtering for geophysical applications, Geophysical Research Letters, 25, 4035–4038, doi:10.1029/1998GL900033, 1998.

Graham, L.: Synthetic interferometer radar for topographic mapping, Proceedings of the IEEE, 62, 763–768, doi:10.1109/PROC.1974.9516, 1974.

Groh, A., Ewert, H., Rosenau, R., Fagiolini, E., Gruber, C., Floricioiu, D., Abdel Jaber, W., Linow, S., Flechtner, F., Eineder, M., Dierking, W., and Dietrich, R.: Mass, Volume and Velocity of the Antarctic Ice Sheet: Present-Day Changes and Error Effects, Surveys in Geophysics, 35, 1481–1505, doi:10.1007/s10712-014-9286-y, 2014.

Hagg, W. J., Braun, L. N., Uvarov, V. N., and Makarevich, K. G.: A comparison of three methods of mass-balance determination in the Tuyuksu

glacier region, Tien Shan, Central Asia, Journal of Glaciology, 50, 505–510, doi:10.3189/172756504781829783, 2004.

Hanssen, R. F.: Radar Interferometry, vol. 2 of *Remote Sensing and Digital Image Processing*, Springer Netherlands, Dordrecht, doi:10.1007/0-306-47633-9, 2001.

Höhle, J., and Höhle, M.: Accuracy assessment of digital elevation models by means of robust statistical methods, ISPRS Journal of Photogrammetry and Remote Sensing 64, 398–406, doi:10.1016/j.isprsjprs.2009.02.003, 2009.

Huss, M.: Density assumptions for converting geodetic glacier volume change to mass change, The Cryosphere, 7, 877–887, doi:10.5194/tc-7-877-2013, 2013.

Jaber, W. A., Floricioiu, D., Rott, H., and Eineder, M.: Surface elevation changes of glaciers derived from SRTM and TanDEM–X DEM differences, in: 2013 IEEE International Geoscience and Remote Sensing Symposium - IGARSS, pp. 1893–1896, IEEE, doi:10.1109/IGARSS.2013.6723173, 2013.

Jarvis, A., Reuter, H. I., Nelson, A., and Guevara, E.: Hole-filled SRTM for the globe Version 4, available from the CGIAR–CSI SRTM 90m Database, 2008.

Kääb, A.: Remote Sensing of Mountain Glaciers and Permafrost Creep, Schriftenreihe Physische Geographie, vol. 48, Geographisches Institut der Universität Zürich, Zürich, 2005.

Kääb, A., Berthier, E., Nuth, C., Gardelle, J., and Arnaud, Y.: Contrasting patterns of early twenty-first-century glacier mass change in the Himalayas, Nature, 488, 495–498, doi:10.1038/nature11324, 2012.

Keller, E. A. and DeVecchio, D. E.: Natural Hazards: Earth's Processes as Hazards, Disasters, and Catastrophes, Fourth Edition, Routledge, New York 2016.

Khromova, T. (submitter) and Lavrentiev, I. (analyst): GLIMS Glacier Database, National Snow and Ice Data Center, Boulder Colorado, USA, doi:10.7265/N5V98602, 2006.

Kingslake, J., and Ng, F.: Quantifying the predictability of the timing of jökulhlaups from Merzbacher Lake, Kyrgyzstan, Journal of Glaciology, 59, 805–818, doi:10.3189/2013JoG12J156, 2013.

Kolecka, N. and Kozak, J.: Assessment of the Accuracy of SRTM C– and X–Band High Mountain Elevation Data: a Case Study of the Polish Tatra Mountains, Pure and Applied Geophysics, 171, 897–912, doi:10.1007/s00024-013-0695-5, 2014.

Konovalov, V. G.: Methods for the computations of onset date and daily hydrograph of the outburst from the Mertzbacher Lake, Tien-shan, in: Hydrology in Mountainous Regions. I - Hydrological Measurements; the Water Cycle (Proceedings of two Lausanne Symposia, August 1990), No. 193. pp. 181–188, 1990.

Krieger, G., Zink, M., Bachmann, M., Bräutigam, B., Schulze, D., Martone, M., Rizzoli, P., Steinbrecher, U., Walter Antony, J., De Zan, F., Hajnsek, I., Papathanassiou, K., Kugler, F., Rodriguez Cassola, M., Younis, M., Baumgartner, S., López-Dekker, P., Prats, P., and Moreira, A.: TanDEM-X: A radar interferometer with two formation-flying satellites, Acta Astronautica, 89, 83–98, doi:10.1016/j.actaastro.2013.03.008, 2013.

Li, J., Li, Z., Zhu, J., Ding, X., Wang, C., and Chen, J.: Deriving surface motion of mountain glaciers in the Tuomuer-Khan Tengri Mountain Ranges from PALSAR images, Global and Planetary Change, 101, 61–71, doi:10.1016/j.gloplacha.2012.12.004, 2013.

Li, J., Li, Z., Ding, X, Wang, Q., Zhu, J., and Wang, C.: Investigating mountain glacier motion with the method of SAR intensity-tracking: Removal of topographic effects and analysis of the dynamic patterns, Earth-Science Reviews, 138, 179–195, doi:10.1016/j.earscirev.2014.08.016, 2014.

Ludwig, R. and Schneider, P.: Validation of digital elevation models from SRTM X–SAR for applications in hydrologic modeling, ISPRS Journal of Photogram-

metry and Remote Sensing, 60, 339–358, doi:10.1016/j.isprsjprs.2006.05.003, 2006.

Marschalk, U., Roth, A., Eineder, M., and Suchandt, S.: Comparison of DEMs derived from SRTM / X– and C–band, in: IEEE International IEEE International IEEE International Geoscience and Remote Sensing Symposium, 2004. IGARSS '04. Proceedings. 2004, vol. 7, pp. 4531–4534, IEEE, doi:10.1109/IGARSS.2004.1370162, 2004.

Mayer, C., Lambrecht, A., Hagg, W., Helm, A., and Scharrer, K.: Post-drainage ice dam response at Lake Merzbacher, Inylchek Glacier, Kyrgyzstan, Geografiska Annaler, Series A: Physical Geography, 90, 87–96, doi:10.1111/j.1468-0459.2008.00336.x, 2008.

Mayr, E., Juen, M., Mayer, C., Usubaliev, R., and Hagg, W. J.: Modeling Runoff from the Inylchek glaciers and Filling of Ice-Dammed Lake Merzbacher, Central Tian Shan, Geografiska Annaler, Series A: Physical Geography, 96, 609–625, doi:10.1111/geoa.12061, 2014.

Neckel, N., Braun, A., Kropáček, J., and Hochschild, V.: Recent mass balance of the Purogangri Ice Cap, central Tibetan Plateau, by means of differential X–band SAR interferometry, The Cryosphere, 7, 1623–1633, doi:10.5194/tc-7-1623-2013, 2013.

Neelmeijer, J., Motagh, M., and Wetzel, H.-U.: Estimating Spatial and Temporal Variability in Surface Kinematics of the Inylchek Glacier, Central Asia, using TerraSAR–X Data, Remote Sensing, 6, 9239–9259, doi:10.3390/rs6109239, 2014.

Ng, F., and Liu, S.: Temporal dynamics of a jökulhlaup system, Journal of Glaciology, 55, 651–665, doi:10.3189/002214309789470897, 2009.

Ng, F., Liu, S., Mavlyudov, B., and Wang, Y.: Climatic control on the peak discharge of glacier outburst floods, Geophysical Research Letters, 34, 1–5, doi:10.1029/2007GL031426, 2007.

Nobakht, M., Motagh, M., Wetzel, H.-U., Roessner, S., and Kaufmann, H.: The Inylchek Glacier in Kyrgyzstan, Central Asia: Insight on Surface Kinematics from Optical Remote Sensing Imagery, Remote Sensing, 6, 841–856, doi:10.3390/rs6010841, 2014.

Nuth, C. and Kääb, A.: Co-registration and bias corrections of satellite elevation data sets for quantifying glacier thickness change, The Cryosphere, 5, 271–290, doi:10.5194/tc-5-271-2011, 2011.

Osmonov, A., Bolch, T., Xi, C., Kurban, A., and Guo, W.: Glacier characteristics and changes in the Sary-Jaz River Basin (Central Tien Shan, Kyrgyzstan) – 1990–2010, Remote Sensing Letters, 4, 725–734, doi:10.1080/2150704X.2013.789146, 2013.

Pandey, P. and Venkataraman, G.: Comparison of DEMs derived from TanDEM–X and SRTM–C for Himalayan terrain, in: 2013 IEEE International Geoscience and Remote Sensing Symposium - IGARSS, pp. 322–325, IEEE, doi:10.1109/IGARSS.2013.6721157, 2013.

Paul, F.: Calculation of glacier elevation changes with SRTM: Is there an elevation-dependent bias?, Journal of Glaciology, 54, 945–946, doi:10.3189/002214308787779960, 2008.

Paul, F. and Haeberli, W.: Spatial variability of glacier elevation changes in the Swiss Alps obtained from two digital elevation models, Geophysical Research Letters, 35, L21 502, doi:10.1029/2008GL034718, 2008.

Paul, F., Bolch, T., Kääb, A., Nagler, T., Nuth, C., Scharrer, K., Shepherd, A., Strozzi, T., Ticconi, F., Bhambri, R., Berthier, E., Bevan, S., Gourmelen, N., Heid, T., Jeong, S., Kunz, M., Lauknes, T. R., Luckman, A., Merryman Boncori, J. P., Moholdt, G., Muir, A., Neelmeijer, J., Rankl, M., VanLooy, J., and Van Niel, T.: The glaciers climate change initiative: Methods for creating glacier area, elevation change and velocity products, Remote Sensing of Environment, 162, 408–426, doi:10.1016/j.rse.2013.07.043, 2015.

Pfeffer, W. T., Arendt, A. A., Bliss, A., Bolch, T., Cogley, J. G., Gardner, A. S., Hagen, J.-O., Hock, R., Kaser, G., Kienholz, C., Miles, E. S., Moholdt, G., Mölg, N., Paul, F., Radić, V., Rastner, P., Raup, B. H., Rich, J., and Sharp, M. J.: The Randolph Glacier Inventory: a globally complete inventory of glaciers, Journal of Glaciology, 60, 537–552, doi:10.3189/2014JoG13J176, 2014.

Pieczonka, T. and Bolch, T.: Region-wide glacier mass budgets and area changes for the Central Tien Shan between ~1975 and 1999 using Hexagon KH–9 imagery, Global and Planetary Change, 128, 1–13, doi:10.1016/j.gloplacha.2014.11.014, 2015.

Pieczonka, T., Bolch, T., Junfeng, W., and Shiyin, L.: Heterogeneous mass loss of glaciers in the Aksu-Tarim Catchment (Central Tien Shan) revealed by 1976 KH–9 Hexagon and 2009 SPOT–5 stereo imagery, Remote Sensing of Environment, 130, 233–244, doi:10.1016/j.rse.2012.11.020, 2013.

Racoviteanu, A. E., Manley, W. F., Arnaud, Y., and Williams, M. W.: Evaluating digital elevation models for glaciologic applications: An example from Nevado Coropuna, Peruvian Andes, Global and Planetary Change, 59, 110–125, doi:10.1016/j.gloplacha.2006.11.036, 2007.

Rankl, M. and Braun, M.: Glacier elevation and mass changes over the central Karakoram region estimated from TanDEM–X and SRTM/X–SAR digital elevation models, Annals of Glaciology, 51, 273–281, doi:10.3189/2016AoG71A024, 2016.

Raup, B., Racoviteanu, A., Khalsa, S. J. S., Helm, C., Armstrong, R., and Arnaud, Y.: The GLIMS geospatial glacier database: A new tool for studying glacier change, Global and Planetary Change, 56, 101–110, doi:10.1016/j.gloplacha.2006.07.018, 2007.

Rignot, E., Echelmeyer, K., and Krabill, W.: Penetration depth of interferometric synthetic-aperture radar signals in snow and ice, Geophysical Research Letters, 28, 3501–3504, doi:10.1029/2000GL012484, 2001.

Rosen, P. A., Werner, C. W., and Hiramatsu, A.: Two-dimensional phase unwrapping of SAR interferograms by charge connection through neutral trees, Proceedings IGARSS'94, Pasadena, 8.–12. August, 1994.

Rott, H., Floricioiu, D., Wuite, J., Scheiblauer, S., Nagler, T., and Kern, M.: Mass changes of outlet glaciers along the Nordensjköld Coast, northern Antarctic Peninsula, based on TanDEM–X satellite measurements, Geophysical Research Letters, 41, 8123–8129, doi:10.1002/2014GL061613, 2014.

Seehaus, T., Marinsek, S., Helm, V., Skvarca, P., and Braun, M.: Changes in ice dynamics, elevation and mass discharge of Dinsmoor–Bombardier–Edgeworth glacier system, Antarctic Peninsula, Earth and Planetary Science Letters, 427, 125–135, doi:10.1016/j.epsl.2015.06.047, 2015.

Shangguan, D. H., Bolch, T., Ding, Y. J., Kröhnert, M., Pieczonka, T., Wetzel, H. U., and Liu, S. Y.: Mass changes of Southern and Northern Inylchek Glacier, Central Tian Shan, Kyrgyzstan, during ~1975 and 2007 derived from remote sensing data, The Cryosphere, 9, 703–717, doi:10.5194/tc-9-703-2015, 2015.

Vijay, S., and Braun, M.: Elevation Change Rates of Glaciers in the Lahaul-Spiti (Western Himalaya, India) during 2000–2012 and 2012–2013, Remote Sensing, 8, 1038, doi:10.3390/rs8121038, 2016.

Wendleder, A., Felbier, A., Wessel, B., Huber, M., and Roth, A.: A Method to Estimate Long-Wave Height Errors of SRTM C–Band DEM, IEEE Geoscience and Remote Sensing Letters, 13, 5, 696–700, doi:10.1109/LGRS.2016.2538822, 2016.

Werner, C. L., Wegmüller, U., Strozzi, T., and Wiesmann, A.: Gamma SAR and interferometric processing software, in: Proceedings of ERS–ENVISAT Symposium, edited by Sawaya-Lacoste, H., European Space Agency Publications Division, Noordwijk, Gothenburg, Sweden, 2001.

Wuite, J., Rott, H., Hetzenecker, M., Floricioiu, D., De Rydt, J., Gudmundsson, G. H., Nagler, T., and Kern, M.: Evolution of surface velocities and ice discharge of Larsen B outlet glaciers from 1995 to 2013, The Cryosphere, 9, 957–969, doi:10.5194/tc-9-957-2015, 2015.

Yan, S., Guo, H., Liu, G., and Ruan, Z.: Mountain glacier displacement estimation using a DEM-assisted offset tracking method with ALOS/PALSAR data, Remote Sensing Letters, 4, 494–503, doi:10.1080/2150704X.2012.754561, 2013.

Zech, C., Schöne, T., Neelmeijer, J., Zubovich, A., and Galas, R.: Geodetic Monitoring Networks: GNSS-Derived Glacier Surface Velocities at the Global Change Observatory Inylchek (Kyrgyzstan), in: Proceedings of the IAG General Assembly 2013. International Association of Geodesy Symposia, Potsdam, pp. 557–563, doi:10.1007/1345_2015_38, 2015.

Zech, C., Schöne, T., Neelmeijer, J., and Zubovich, A.: Continuous Kinematic GPS Monitoring of a Glacier Lake Outburst Flood, in: Proceedings of the IUGG General Assembly 2015. International Association of Geodesy Symposia, Prague, *accepted*, 2016.

Zemp, M., Thibert, E., Huss, M., Stumm, D., Rolstad Denby, C., Nuth, C., Nussbaumer, S. U., Moholdt, G., Mercer, A., Mayer, C., Joerg, P. C., Jansson, P., Hynek, B., Fischer, A., Escher-Vetter, H., Elvehøy, H., and Andreassen, L. M.: Reanalysing glacier mass balance measurement series, The Cryosphere, 7, 1227–1245, doi:10.5194/tc-7-1227-2013, 2013.

Zwally, H. J., Schutz, R., Bentley, C., Bufton, J., Herring, T., Minster, J., Spinhirne, J., and Thomas, R.: GLAS/ICESat L2 Global Land Surface Altimetry Data, Version 34, Tech. rep., NASA National Snow and Ice Data Center Distributed Active Archive Center, Boulder Colorado, USA, doi:10.5067/ICESAT/GLAS/DATA227, 2014.